

Design and Modeling of a Six-Bar Mechanism for Repetitive Tasks with Symmetrical End-Effector Motion

Eddie Gazo-Hanna

College of Engineering and Technology, American University of the Middle East, Egaila 54200, Kuwait
eddie-hanna@aum.edu.kw (corresponding author)

Ahmed Saber

College of Engineering and Technology, American University of the Middle East, Egaila 54200, Kuwait
ahmed.saber@aum.edu.kw

Semaan Amine

College of Engineering and Technology, American University of the Middle East, Egaila 54200, Kuwait
semaan.amine@aum.edu.kw

Received: 14 June 2024 | Revised: 10 July 2024 | Accepted: 13 July 2024

Licensed under a CC-BY 4.0 license | Copyright (c) by the authors | DOI: <https://doi.org/10.48084/etasr.8139>

ABSTRACT

This study investigates the dynamics of a novel planar six-bar mechanism with one Degree of Freedom (DoF), incorporating both four-bar and five-bar linkages. Kinematic analysis is performed by setting up closed-loop equations, and the results are validated against SOLIDWORKS software simulations. Additionally, a static stress analysis assesses the structural integrity of the mechanism under operational loads, identifying potential failure points and ensuring design adequacy. Dynamic force analysis is then performed to determine the driving torque of the actuator for the designed amphibious mechanism. These findings highlight the mechanism's potential for precise motion control in compact applications, providing valuable insights into its practical utility in various industrial applications.

Keywords-six-bar linkage; static analysis; robotics; planar mechanism

I. INTRODUCTION

Recently, with the rapid development of parallel robotics and controllable mechanisms, planar mechanisms have become increasingly used in mechanical design [1-4]. Among these, the six-bar one Degree of Freedom (DoF) mechanisms are particularly notable. These mechanisms are fundamental components of many mechanical systems that require complex motion paths or force outputs. Typically comprising six moving links, including the input and ground links, these mechanisms provide a single controlled movement, while the rest of the system follows a predetermined path or sequence. In general, six-bar mechanisms possessing a single DoF can be categorized into two distinct types: Watt's six-bar linkage [5, 6], which is used to transform rotary motion into an approximately straight line, and Stephenson's six-bar linkage [6, 7], often utilized in foldable machinery and multi-link suspension systems in vehicles. These mechanisms are highly valued for their ability to deliver precise motion control in compact spaces, making them indispensable in both industrial and consumer applications.

Watt's mechanism, also known as Watt's linkage, is a type of mechanical linkage in which the central moving point is constrained to travel a nearly straight path. It was used in the Watt steam engine, in automobile suspensions as a lateral guiding mechanism, and in various applications in robotics [8]. There are two primary types of Watt mechanisms. The first, Watt's Straight-Line Mechanism, also called Watt's linkage, is used to guide the piston of steam engines through a straight-line path. It is one of the simplest mechanisms to generate close-to-straight-line motion for a considerable distance. The second type is the Watt-I mechanism, which can operate in eight different combinations of assembly modes and output links [9]. The Stephenson mechanism is another type of six-bar linkage that is used in various engineering applications. It consists of one four-bar loop and one five-bar loop, with two ternary links that are separated by a binary link. This means that the two ternary links are not connected by a joint, unlike in the Watt topology [8]. Stephenson I is characterized by two ternary links and four binary links. It is often utilized in applications where a specific motion path is required. Stephenson II has one ternary link, one quaternary link, and four binary links and is commonly used in applications where

straight-line motion is required. Stephenson III is characterized by two quaternary links and four binary links, while the end of the second ternary link can be implemented as an end effector [9]. It is often employed in applications where complex motion paths are required and is extremely beneficial for creating versatile mechanical devices, including robotic joints and surgical tools [10-14].

The Stephenson III mechanism can be deployed in various industrial applications where precise controlled movement within a limited workspace is crucial. For instance, it can be used in the assembly of Printed Circuit Boards (PCBs), where components must be accurately placed at high speeds. This mechanism can also find application as micromanipulators mounted on the end-effectors of larger slower serial manipulators, facilitating delicate operations that require finer control. Furthermore, it can enhance efficiency and accuracy in high-speed, high-precision milling machines and automated drilling machines. In addition to these applications, its precise control [10, 11] makes it ideal for use in precision surface finish measuring machines and as a path tracker in automated welding machines. Its adaptability can also be demonstrated in commercial pick-and-place robots that demand rapid and accurate handling of various objects. In robotics, it can be employed to generate walking gaits in biped robots and swimming gaits in swimming robots, showcasing its utility in mimicking complex locomotive patterns. This mechanism can also find application in automatic planar measuring devices, where precise and reliable movement is essential.

Despite numerous existing studies on the inversions of Stephenson mechanisms, a significant gap remains in understanding the specific inversion of the Stephenson III mechanism for repetitive tasks. The present study addresses this gap by conducting an in-depth exploration of the kinematic and dynamic attributes of the mechanism. This study not only provides detailed theoretical insights, but also validates these findings through CAD software simulations. Another novel aspect is the integration of dynamic analysis to determine the required driving torque, a feature often overlooked in previous studies. Overall, the current study aims to provide valuable insights to facilitate the practical application of this mechanism by combining kinematic analysis with static and dynamic force analyses, offering a comprehensive understanding of its performance.

Initially, a comprehensive kinematic analysis is performed using the closed-loop method. This analysis includes detailed examinations of the position, velocity, and acceleration of all components of the mechanism through an algebraic approach, resulting in the derivation of equations governing the end effector's position, velocity, and acceleration. The equations developed from the closed-loop equations are subsequently compared with the results obtained from simulations conducted using the SOLIDWORKS software. This simulation is instrumental in visualizing the mechanism's dynamics, and the comparative analysis helps validate the analytical models. The results of this simulation, along with a detailed discussion of the findings, elucidate the mechanism's kinematic behavior and its implications for practical applications.

After establishing the kinematic feasibility of the selected six-bar mechanism, it is crucial to analyze its structural load. This involves performing a static stress analysis to evaluate the mechanism's structural integrity under various operating conditions. Static stress analysis was carried out at two critical crank positions using SOLIDWORKS. By examining the stress distributions, potential points of failure are identified and design strength criteria are assessed. Such an analysis is indispensable for reliability and safety considerations. Following static stress analysis, a dynamic force analysis is performed to understand the forces and torques that act on the mechanism during its operation, which can significantly influence its performance and longevity.

II. DESCRIPTION OF THE PROPOSED MECHANISM

Figure 1 illustrates the selected planar single DoF six-bar mechanism, incorporating both a four-bar (O_2ABO_4) and a five-bar (O_2ACDO_6) linkages, with the ternary link (ABC) being common to both. To optimize the mechanism, the genetic algorithm was used to determine the optimal dimensions of the various links. Additionally, through the appropriate rotation of the actuating crank (O_2A), the characteristic point G of the mechanism was enabled to follow a desired planar trajectory.

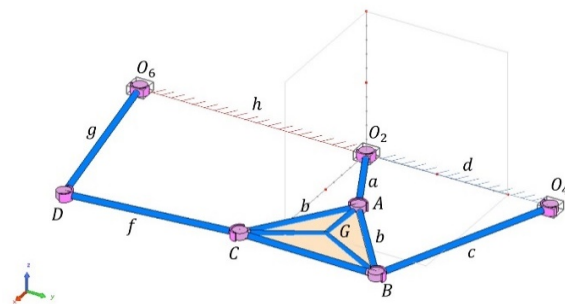


Fig. 1. Scheme of the proposed mechanism.

III. KINEMATIC ANALYSIS

The kinematic analysis is carried out assuming a constant crank rotation ($\omega_2 = 0.5 \text{ rad/s}, \alpha_2 = 0 \text{ rad/s}^2$). An X-Y reference coordinate system is set up with its origin at point O_2 (Figure 2), and the orientation of the links is defined by an angle measured in the counterclockwise direction with respect to the horizontal X-axis.

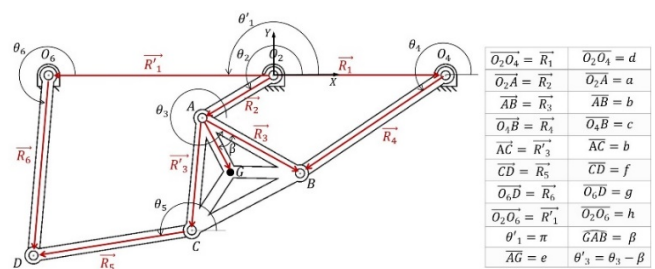


Fig. 2. Vector loops of the mechanism considered for synthesis.

A. Position Analysis

The vector loop equation of the four-bar O_2ABO_4 can be written as:

$$\vec{R}_2 + \vec{R}_3 - \vec{R}_4 - \vec{R}_1 = \vec{0} \quad (1)$$

To simplify the notation and minimize the use of subscripts, the scalar lengths are denoted a , b , c , and d . The equation then becomes:

$$ae^{j\theta_2} + be^{j\theta_3} - ce^{j\theta_4} - de^{j\theta_1} = 0 \quad (2)$$

$$\theta_3 = 2 \tan^{-1} \left(\frac{-E \pm \sqrt{E^2 - 4DF}}{2D} \right) \quad (3)$$

$$\theta_4 = 2 \tan^{-1} \left(\frac{-B \pm \sqrt{B^2 - 4AC}}{2A} \right) \quad (4)$$

where:

$$A = -k_1 + \cos \theta_2 - k_2 \cos \theta_2 + k_3 \quad (5)$$

$$B = -2 \sin \theta_2 \quad (6)$$

$$C = k_1 - (k_2 + 1) \cos \theta_2 + k_3 \quad (7)$$

$$D = -k_1 + (k_4 + 1) \cos \theta_2 + k_5 \quad (8)$$

$$E = -2 \sin \theta_2 \quad (9)$$

$$F = k_1 + (k_4 - 1) \cos \theta_2 + k_5 \quad (10)$$

$$k_1 = \frac{d}{a}; \quad k_2 = \frac{d}{c}; \quad k_3 = \frac{a^2 - b^2 + c^2 + d^2}{2ac} \quad (11)$$

$$k_4 = \frac{d}{b}; \quad k_5 = \frac{c^2 - a^2 - b^2 - d^2}{2ab} \quad (12)$$

The second loop (O_2ACDO_6) equation can be written as:

$$\vec{R}_2 + \vec{R}'_3 + \vec{R}_5 - \vec{R}_6 - \vec{R}'_1 = \vec{0} \quad (13)$$

To simplify the notation and minimize the use of subscripts, the scalar lengths are denoted as a , b , f , g , and h . This equation then becomes:

$$ae^{j\theta_2} + be^{j\theta_3} + fe^{j\theta_5} - ge^{j\theta_6} - he^{j\theta_1} = 0 \quad (14)$$

where:

$$\theta'_3 = \theta_3 - \gamma \quad \text{and} \quad \theta'_1 = \pi \quad (15)$$

Similar to (2), this equation leads to two scalar equations that can be solved simultaneously for θ_5 and θ_6 :

$$\theta_5 = 2 \tan^{-1} \left(\frac{-F' \pm \sqrt{F'^2 - 4E'D'}}{2E'D'} \right) \quad (16)$$

$$\theta_6 = 2 \tan^{-1} \left(\frac{-K \pm \sqrt{K^2 - 4LJ}}{2J} \right) \quad (17)$$

where:

$$E' = C' - A' \quad F' = 2B' \quad \text{and} \quad D' = C' + A' \quad (18)$$

$$J = I - G \quad K = 2H \quad \text{and} \quad L = I + G \quad (19)$$

$$A' = 2fh + 2af \cos \theta_2 + 2b \cos \theta_3' \quad (20)$$

$$B' = 2af \sin \theta_2 + 2bf \sin \theta_3' \quad (21)$$

$$C' = a^2 + b^2 + f^2 + h^2 - g^2 + 2ab \cos(\theta_2 - \theta_3') + 2abh \cos \theta_2 + 2abh \cos \theta_3' \quad (22)$$

$$G = -(2gh + 2ag \cos \theta_2 + 2bg \cos(\theta_3')) \quad (23)$$

$$H = -(2ag \sin \theta_2 + 2bg \sin(\theta_3')) \quad (24)$$

$$I = a^2 + b^2 + g^2 + h^2 - f^2 + 2ab \cos(\theta_2 - \theta_3') + 2ah \cos \theta_2 + 2bh \cos \theta_3' \quad (25)$$

The vector position equation of the end effector point G can be written in the following form:

$$\vec{R}_G = \vec{O}_2\vec{A} + \vec{AG} \quad (26)$$

By expanding this expression and separating the real and imaginary parts, the coordinates of the end effector point G_x and G_y are obtained:

$$G_x = a \cos \theta_2 + e \cos(\theta_3 - \beta) \quad (27)$$

$$G_y = a \sin \theta_2 + e \sin(\theta_3 - \beta) \quad (28)$$

B. Velocity Analysis

To get an expression for the angular velocities of links 3 and 4, (2) is differentiated with respect to time, becoming:

$$ja\omega_2 e^{j\theta_2} + jb\omega_3 e^{j\theta_3} - jc\omega_4 e^{j\theta_4} = 0 \quad (29)$$

This equation leads to two scalar equations, which can be solved simultaneously for ω_3 and ω_4 :

$$\omega_3 = \frac{a\omega_2 \sin(\theta_4 - \theta_2)}{b \sin(\theta_3 - \theta_4)} \quad (30)$$

$$\omega_4 = \frac{a\omega_2 \sin(\theta_2 - \theta_3)}{c \sin(\theta_4 - \theta_3)} \quad (31)$$

To get an expression for the angular velocities of links 5 and 6, (14) is differentiated with respect to time, becoming:

$$ja\omega_2 e^{j\theta_2} + jb\omega_3 e^{j\theta'_3} - jf\omega_5 e^{j\theta_5} + jg\omega_6 e^{j\theta_6} = 0 \quad (32)$$

This equation leads to two scalar equations that can be solved simultaneously for ω_5 and ω_6 :

$$\omega_5 = \frac{a\omega_2 \sin(\theta_6 - \theta_2)}{f \sin(\theta_5 - \theta_6)} + \frac{b\omega_3 \sin(\theta_6 - \theta'_3)}{f \sin(\theta_5 - \theta_6)} \quad (33)$$

$$\omega_6 = \frac{a\omega_2 \sin(\theta_5 - \theta_2)}{g \sin(\theta_5 - \theta_6)} + \frac{b\omega_3 \sin(\theta_5 - \theta'_3)}{g \sin(\theta_5 - \theta_6)} \quad (34)$$

The velocity components of the end effector point G are calculated by numerical differentiation of the position equation (25):

$$v_{G_x} = -a\omega_2 \sin \theta_2 - e\omega_2 \sin(\theta_3 - \beta) \quad (35)$$

$$v_{G_y} = a\omega_2 \cos \theta_2 + e\omega_2 \cos(\theta_3 - \beta) \quad (36)$$

C. Acceleration Analysis

To get an expression for the angular accelerations of links 3 and 4, (29) is differentiated with respect to time, becoming:

$$(-a\omega_2^2 e^{j\theta_2}) + (b\alpha_3 j e^{j\theta_3} - b\omega_3^2 e^{j\theta_3}) - (c\alpha_4 j e^{j\theta_4} - c\omega_4^2 e^{j\theta_4}) = 0 \quad (37)$$

This equation leads to two scalar equations that can be solved simultaneously for α_3 and α_4 :

$$\alpha_3 = \frac{OP-MR}{MQ-NP} \quad (38)$$

$$\alpha_4 = \frac{OQ-NR}{MQ-NP} \quad (39)$$

where:

$$\begin{aligned} M &= c \sin \theta_4 \\ N &= b \sin \theta_3 \\ O &= a\alpha_2 \sin \theta_2 + a\omega_2^2 \cos \theta_2 + \\ & b\omega_3^2 \cos \theta_3 - c\omega_4^2 \cos \theta_4 \\ P &= c \cos \theta_4 \\ Q &= b \cos \theta_3 \\ R &= a\alpha_2 \cos \theta_2 - a\omega_2^2 \sin \theta_2 - b\omega_3^2 \sin \theta_3 \\ & + c\omega_4^2 \sin \theta_4 \end{aligned} \quad (40)$$

To get an expression for the angular accelerations of links 5 and 6, (32) is differentiated with respect to time and becomes:

$$\begin{aligned} & (a\alpha_2 j e^{j\theta_2} - a\omega_2^2 e^{j\theta_2}) + (b\alpha_3 j e^{j\theta_3} - b\omega_3^2 e^{j\theta_3}) \\ & + (f\alpha_5 j e^{j\theta_5} - f\omega_5^2 e^{j\theta_5}) \\ - (g\alpha_6 j e^{j\theta_6} - g\omega_6^2 e^{j\theta_6}) & = 0 \end{aligned} \quad (41)$$

This equation leads to two scalar equations that can be solved simultaneously for α_5 and α_6 :

$$\alpha_5 = \frac{1}{f \sin(\theta_6 - \theta_5)} [a\alpha_2 \sin(\theta_2 - \theta_6) + a\omega_2^2 \cos(\theta_6 - \theta_2) + b\alpha_3 \sin(\theta_3 - \theta_6) + b\omega_3^2 \cos(\theta_6 - \theta_3) + f\omega_5^2 \cos(\theta_6 - \theta_5) - g\omega_6^2] \quad (42)$$

$$\alpha_6 = \frac{1}{g \sin(\theta_6 - \theta_5)} [a\alpha_2 \sin(\theta_2 - \theta_5) + a\omega_2^2 \cos(\theta_5 - \theta_2) + b\alpha_3 \sin(\theta_3 - \theta_5) + b\omega_3^2 \cos(\theta_5 - \theta_3) + f\omega_5^2 - g\omega_6^2 \cos(\theta_6 - \theta_5)] \quad (43)$$

The acceleration components of the end effector point G are calculated by numerical differentiation:

$$a_{G_x} = -a\alpha_2 \sin \theta_2 - a\omega_2^2 \cos \theta_2 - e\alpha_3 \sin(\theta_3 - \beta) - e\omega_3^2 \cos(\theta_3 - \beta) \quad (44)$$

$$a_{G_y} = a\alpha_2 \cos \theta_2 - a\omega_2^2 \sin \theta_2 + e\alpha_3 \cos(\theta_3 - \beta) - e\omega_3^2 \sin(\theta_3 - \beta) \quad (45)$$

IV. DYNAMIC FORCE ANALYSIS

To determine the internal forces and torque in the system, dynamic force analysis is performed using Newton's laws as defined in (46) and (47):

$$\sum \vec{F} = m\vec{a}_G \quad (46)$$

$$\sum \vec{T} = I_G \alpha \quad (47)$$

These equations are projected in the rectangular coordinate system, leading to three scalar equations (48):

$$\sum F_x = ma_{G_x}, \quad \sum F_y = ma_{G_y}, \quad \sum T = I_G \alpha \quad (48)$$

where, for each link, m is the mass, a_{G_x} and a_{G_y} are the linear accelerations of the center of mass, I_G is the mass moment of inertia calculated at the center of mass, and α is the angular acceleration. These three equations are written for each moving body in the system, using the free-body diagrams in Figure 3. This results in a set of linear simultaneous equations, which are solved using a matrix method.

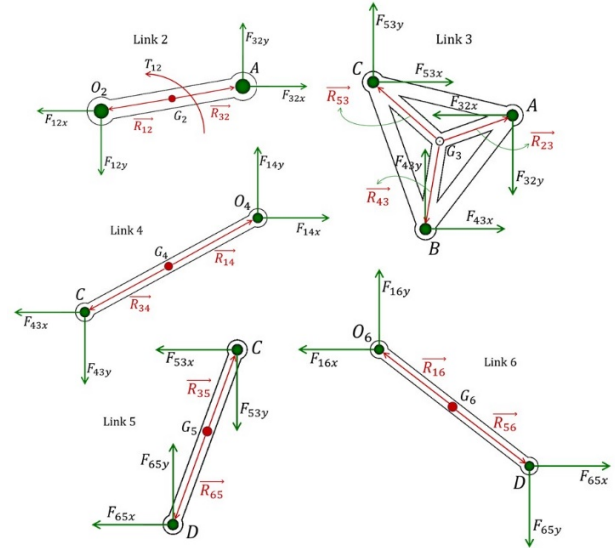


Fig. 3. Free body diagrams of each link.

Fifteen equations have been developed to determine fifteen unknowns: the forces F_{12x} , F_{12y} , F_{32x} , F_{32y} , F_{43x} , F_{43y} , F_{53x} , F_{53y} , F_{14x} , F_{14y} , F_{16x} , F_{16y} , F_{65x} , F_{65y} , and the input torque T_{12} . The dimensions of the link lengths and positions, the locations of the links' Centers of Gravity (CGs), the linear accelerations of those CGs, and the angular accelerations and velocities of the links are all determined through kinematic analysis. These equations can now be used to assemble the matrices and find the solutions, as in (49).

V. DIMENSIONAL SYNTHESIS

The dimensional synthesis of a linkage involves determining the lengths of the links necessary to accomplish the desired motions. This process can be a form of quantitative synthesis if an algorithm is defined for the particular problem, or it can be a form of qualitative synthesis if there are more variables than equations [15].

In this study, the dimensional synthesis was performed using the GIM software [16, 17], employing the desired path generation method, as evidenced in Figure 4. Path generation is defined as the control of the end effector point in the plane such that it follows a prescribed path. This is typically accomplished with a four-bar crank-rocker or a double-rocker mechanism, wherein a point on the coupler traces the desired output path [15].

$$\begin{bmatrix} F_{12x} \\ F_{12y} \\ F_{32x} \\ F_{32y} \\ F_{43x} \\ F_{43y} \\ F_{53x} \\ F_{53y} \\ F_{14x} \\ F_{14y} \\ F_{65x} \\ F_{65y} \\ F_{16x} \\ F_{16y} \\ T_{12} \end{bmatrix} = \begin{bmatrix} -1 & 0 & 1 & 0 & 0 & 0 & 0 & 0 & 0 & 0 & 0 & 0 & 0 & 0 & 0 \\ 0 & -1 & 0 & 1 & 0 & 0 & 0 & 0 & 0 & 0 & 0 & 0 & 0 & 0 & 0 \\ -R_{12y} & R_{12x} & -R_{32y} & R_{32x} & 0 & 0 & 0 & 0 & 0 & 0 & 0 & 0 & 0 & 0 & 1 \\ 0 & 0 & -1 & 0 & 1 & 0 & 1 & 0 & 0 & 0 & 0 & 0 & 0 & 0 & 0 \\ 0 & 0 & 0 & -1 & 0 & 1 & 0 & 1 & 0 & 0 & 0 & 0 & 0 & 0 & 0 \\ 0 & 0 & R_{23y} & -R_{23x} & R_{43y} & -R_{43x} & -R_{53y} & -R_{53x} & 0 & 0 & 0 & 0 & 0 & 0 & 0 \\ 0 & 0 & 0 & 0 & -1 & 0 & 0 & 0 & 1 & 0 & 0 & 0 & 0 & 0 & 0 \\ 0 & 0 & 0 & 0 & 0 & -1 & 0 & 0 & 0 & 1 & 0 & 0 & 0 & 0 & 0 \\ 0 & 0 & 0 & 0 & -R_{34y} & R_{34x} & 0 & 0 & -R_{14y} & R_{14x} & 0 & 0 & 0 & 0 & 0 \\ 0 & 0 & 0 & 0 & 0 & 0 & -1 & 0 & 0 & 0 & -1 & 0 & 0 & 0 & 0 \\ 0 & 0 & 0 & 0 & 0 & 0 & 0 & 0 & 0 & 0 & 0 & 1 & 0 & 0 & 0 \\ 0 & 0 & 0 & 0 & 0 & 0 & 0 & 0 & 0 & 0 & -R_{65y} & -R_{65x} & 0 & 0 & 0 \\ 0 & 0 & 0 & 0 & 0 & 0 & 0 & 0 & 0 & 0 & 1 & 0 & -1 & 0 & 0 \\ 0 & 0 & 0 & 0 & 0 & 0 & 0 & 0 & 0 & 0 & 0 & -1 & 0 & 1 & 0 \\ 0 & 0 & 0 & 0 & 0 & 0 & 0 & 0 & 0 & R_{56y} & -R_{56x} & R_{16y} & -R_{16x} & 0 & 0 \end{bmatrix}^{-1} \begin{bmatrix} m_2 a_{G2x} \\ m_2 a_{G2y} \\ I_{G2} \alpha_2 \\ m_3 a_{G3x} \\ m_3 a_{G3y} \\ I_{G3} \alpha_3 \\ m_4 a_{G4x} \\ m_4 a_{G4y} \\ I_{G4} \alpha_4 \\ m_5 a_{G5x} \\ m_5 a_{G5y} \\ I_{G5} \alpha_5 \\ m_6 a_{G6x} \\ m_6 a_{G6y} \\ I_{G6} \alpha_6 \end{bmatrix} \quad (49)$$

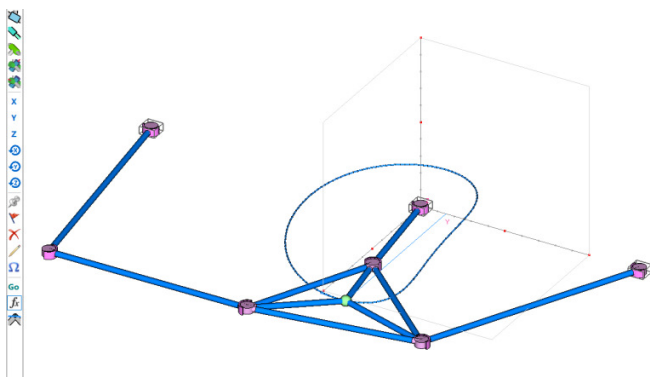


Fig. 4. Dimensional synthesis with desired path motion using GIM.

Table I displays the optimized dimensions obtained from this process.

TABLE I. OPTIMIZED DIMENSIONS OF THE PROPOSED MECHANISM

a	62.6 mm
b	84.8 mm
c	132 mm
d	130 mm
f	121mm
g	136 mm
h	170 mm
e	45.7 mm

VI. STATIC ANALYSIS

The static stress analysis assesses the structural integrity of the mechanism under operational loads, identifying critical failure locations and confirming design suitability. SOLIDWORKS was employed to analyze the stress distribution, deformation, and factor of safety. The six-bar mechanism was designed using SOLIDWORKS, with rectangular bars connected by cylindrical pins, as observed in Figure 5. The dimensions of the bar profile were set at 20×10 mm, while the cylindrical pins had dimensions of Ø10×10 mm. Aluminum 6061 alloy was used as the material for beams [18]. The mechanical properties were obtained from SOLIDWORKS default material properties, as shown in Table II.

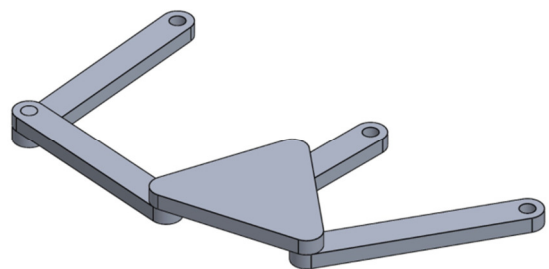


Fig. 5. The six-bar mechanism created using SOLIDWORKS

TABLE II. MECHANICAL PROPERTIES OF ALUMINUM 6061 ALLOY

Elastic Modulus	69000 MPa
Poisson's Ratio	0.33
Shear Modulus	26000 MPa
Mass Density	2700 Kg/m ³
Tensile Strength	124.084 MPa
Yield Strength	55.1485 MPa

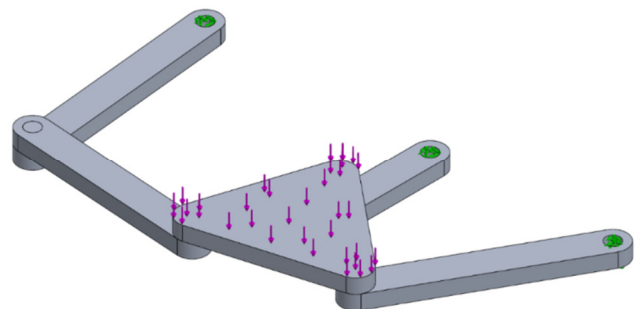


Fig. 6. Load and fixtures. The fixed hinges are represented in green and the load is represented in purple.

The mechanism is set to be fixed at the three hinges O_2 , O_4 , and O_6 . The applied load is oriented vertically downwards, and the mechanism is designed to support a load capacity of 10 kg. Figure 6 depicts the fixed load and the fixtures. The contact between the different parts of the mechanism is set to be bonded. The static stress analysis is conducted on four different crank positions: (1) $\theta_2 = 0^\circ$, (2) $\theta_2 = 90^\circ$, (3) $\theta_2 = 180^\circ$, and (4) $\theta_2 = 270^\circ$. The mesh is automatically generated by SOLIDWORKS using the fine mesh density option as

portrayed in Figure 7. The total number of elements for positions (1), (2), (3), and (4) is determined as 294993, 289385, 293934, and 286660, respectively.



Fig. 7. Mesh structure.

VII. TORQUE ANALYSIS

The driving torque is a crucial design parameter for appropriately sizing the driving motor to ensure reliable and safe operation. The SOLIDWORKS motion analysis package is employed to estimate the driving torque. The six-bar mechanism, created using SOLIDWORKS and exhibited in Figure 5, incorporates a motor at hinge O_2 . The motor's motion is set to a constant speed of 10 RPM. The initial position corresponds to $\theta_2 = 0^\circ$, while the duration of the analysis is 6 s during which the crank completes a full cycle.

VIII. RESULTS AND DISCUSSION

Figure 8 depicts a simulation of the six-bar planar mechanism in operation, highlighting the trajectories generated by the end effector (point G) and point D on the binary link. The traced paths, especially the circular paths by points like G and the linear movement of point D, illustrate the mechanism's capability for precise and variable motion control. This simulation visualizes the dynamic interactions between the links, which are crucial for understanding the mechanism's practical applications in engineering systems.

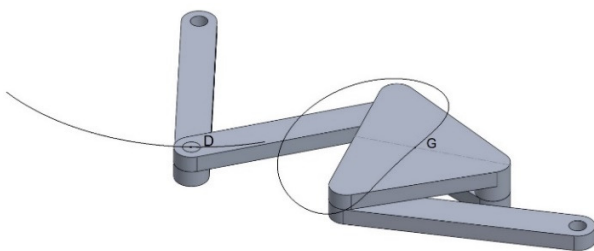


Fig. 8. Motion simulation of the optimized six-bar planar mechanism in operation.

The path of motion of the characteristic point G for the optimized design is presented in Figure 9, showcasing a highly precise and symmetrical loop. The overlaid results from MATLAB and SOLIDWORKS simulations demonstrate exceptional alignment, indicating that the developed position analysis equations result in accurate calculations of the mechanism's motion.

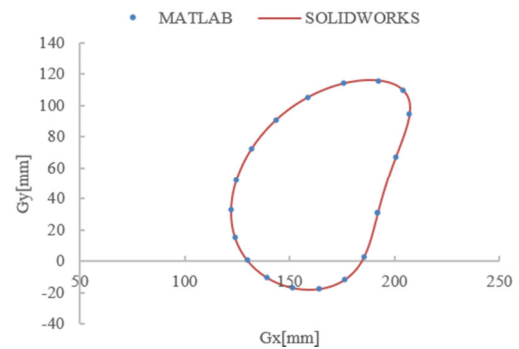


Fig. 9. Path of motion of the characteristic point G.

The velocity diagrams in Figures 10 and 11 can be used to analyze the velocity components of the characteristic point G in the optimized six-bar planar mechanism. The velocity in the X direction exhibits a sinusoidal pattern, showing periodic behavior with crank rotation. This pattern indicates continuous smooth changes in velocity, which are essential for applications requiring precise control over motion. Similarly, the velocity in the Y direction shows sinusoidal behavior. In both figures, the close overlap between MATLAB and SOLIDWORKS simulations confirms that the theoretical calculations and the software simulation outputs are well aligned.

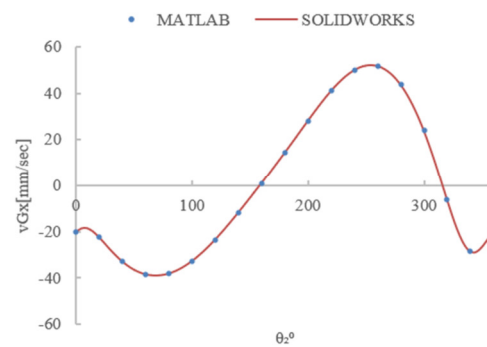


Fig. 10. Velocity of point G for the optimized design in direction X.

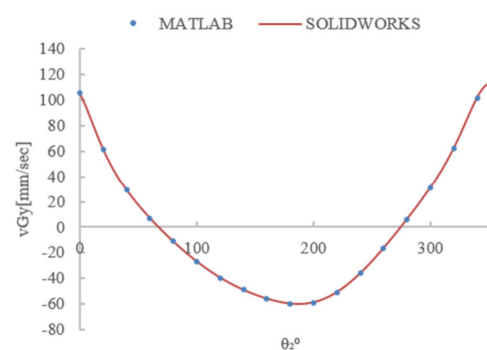


Fig. 11. Velocity of point G for the optimized design in direction Y.

Figures 12 and 13 represent the acceleration of the characteristic point G in the X and Y directions, respectively. Both figures display an excellent correlation between the MATLAB and SOLIDWORKS simulations, confirming their accuracy in predicting the mechanism's behavior.

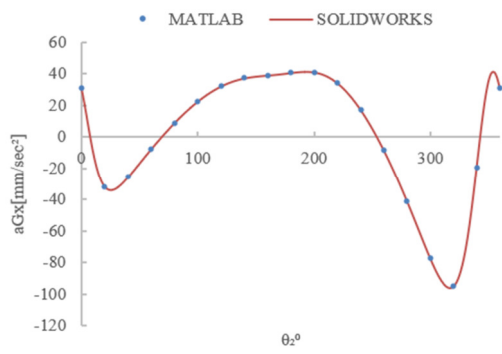


Fig. 12. Acceleration of point G for the optimized design in direction X.

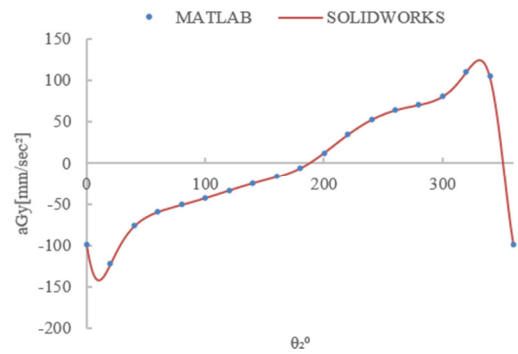


Fig. 13. Acceleration of point G for the optimized design in direction Y.

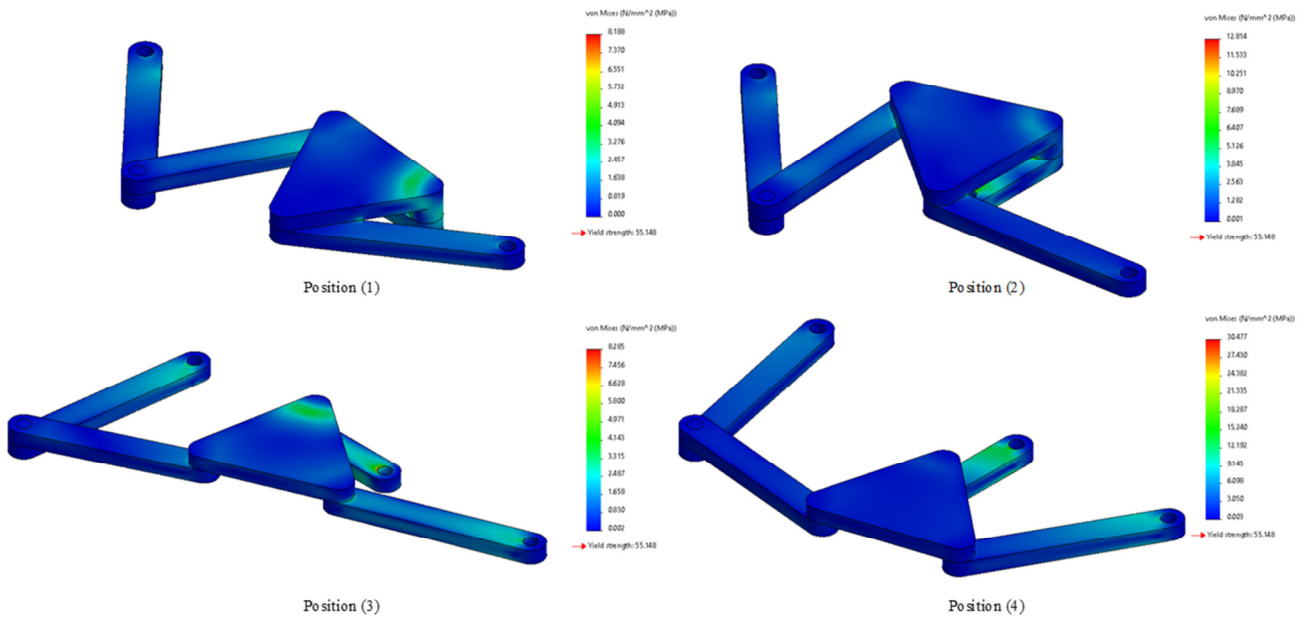


Fig. 14. Stress distribution.

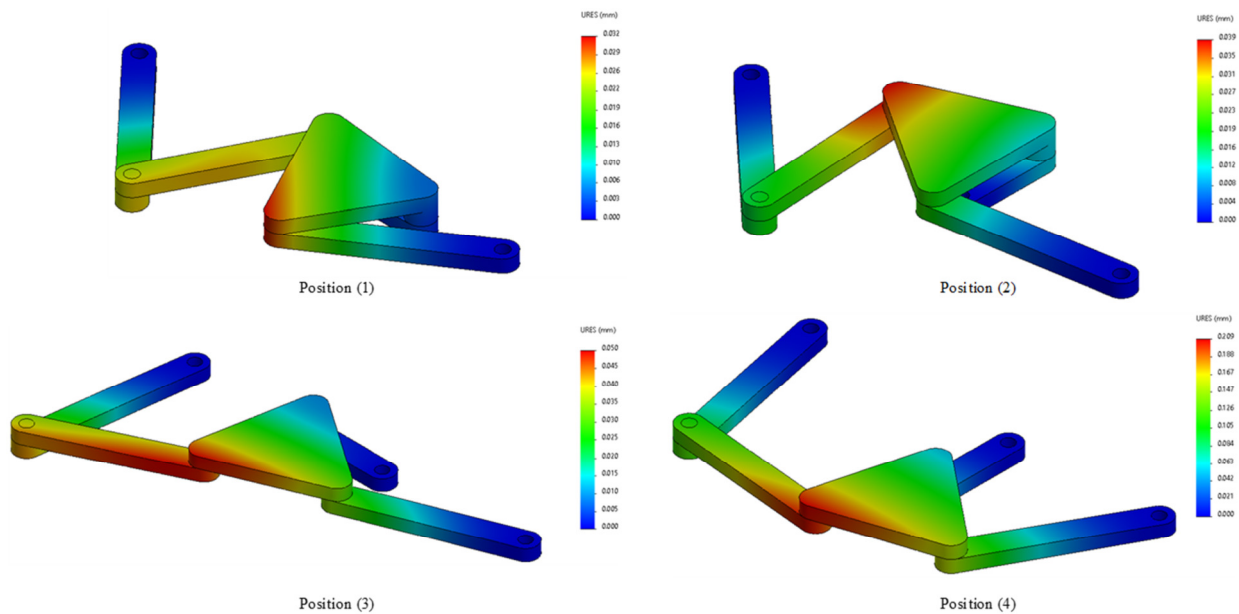


Fig. 15. Deformation distribution.

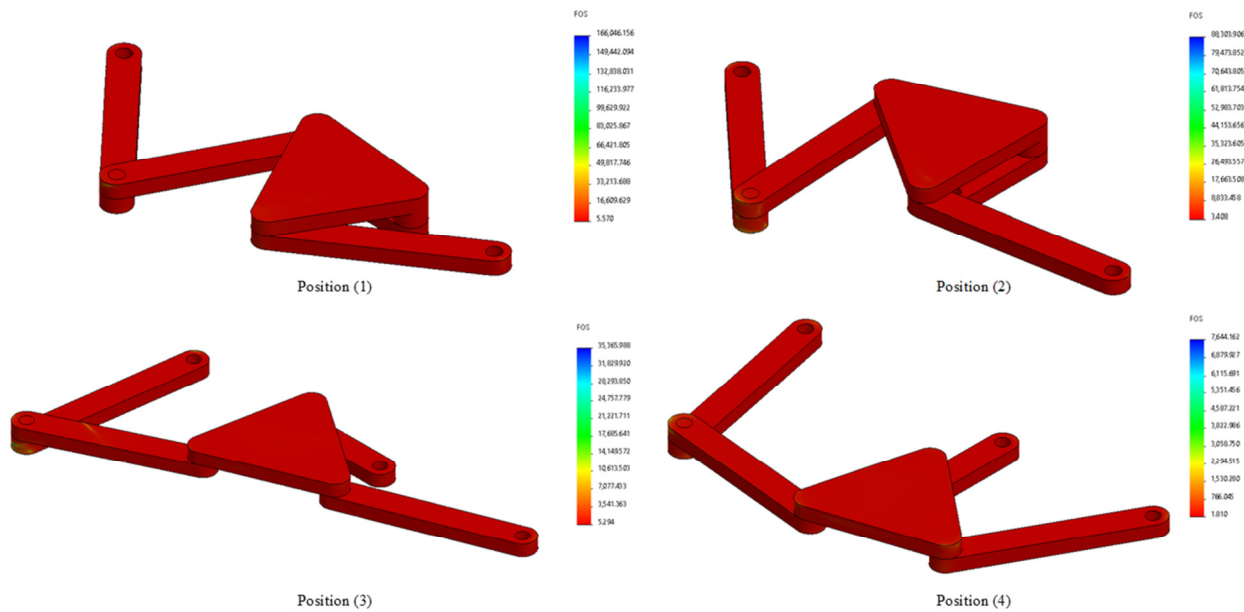


Fig. 16. Factor of safety distribution.

Figure 14 shows the stress distribution within the mechanism. The analysis employs the maximum distortion energy theory, also known as the von Mises-Hencky theory. The maximum stress values at positions (1), (2), (3), and (4) are estimated to be 8.188 MPa, 12.814 MPa, 8.285 MPa, and 30.477 MPa, respectively. Additionally, Figure 15 portrays the deformation occurring in the mechanism elements. The deformation values at positions (1), (2), (3), and (4) are estimated to be 0.032 mm, 0.039 mm, 0.05 mm, and 0.209 mm, respectively. Figure 16 depicts the factor of safety. The factor of safety is defined as the ratio of the yield stress to the maximum stress experienced by the selected component. For positions (1), (2), (3), and (4), the predicted minimum factor of safety values are 5.57, 3.408, 5.294 and 1.81, respectively.

Figure 17 demonstrates the driving torque of the six-bar mechanism, revealing maximum and minimum torque requirements for the drive cycle: 5.46 N·mm and -6.42 N·mm, respectively.

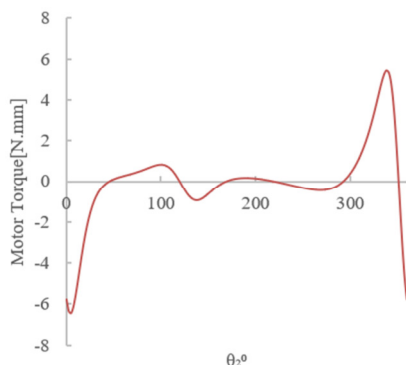


Fig. 17. Driving torque of the six-bar mechanism.

IX. CONCLUSION

This study presented a comprehensive analysis of the Stephenson III mechanism, a six-bar one-DoF mechanism for repetitive tasks with symmetrical end-effector motion. Link dimensions were optimized using the GIM software, and then, a detailed kinematic analysis was performed and validated by SOLIDWORKS software simulations. The results showed precise alignment between theoretical calculations and simulations, confirming the mechanism's capability for precise and variable motion control. The static stress analysis using SOLIDWORKS assessed the structural integrity of the mechanism under operational conditions, revealing stress distribution, deformation, and a satisfactory factor of safety. The findings exhibited that the six-bar mechanism studied has significant potential for various industrial applications. Static stress analysis and dynamic force analysis have further contributed to understanding the structural loads that act on the mechanism and their implications for its performance and longevity. The findings of this study are expected to substantially contribute to the ongoing development and optimization of six-bar one-DoF mechanisms, thereby paving the way for more efficient and reliable mechanical systems. Future work will focus on exploring other inversions of the Stephenson III mechanism and conducting similar analyses to further enhance people's understanding of these mechanisms.

REFERENCES

- [1] M. J. Rider, *Design and Analysis of Mechanisms: A Planar Approach*. Chichester, UK: John Wiley & Sons, 2015.
- [2] K. Zhao, J. P. Schmiedeler, and A. P. Murray, "Design of Planar, Shape-Changing Rigid-Body Mechanisms for Morphing Aircraft Wings," *Journal of Mechanisms and Robotics*, vol. 4, no. 4, Sep. 2012, Art. no. 041007, <https://doi.org/10.1115/1.4007449>.
- [3] S. Amine and E. G. Hanna, "Kinematic Analysis of HALF Parallel Robot," *Journal of Engineering Science and Technology Review*, vol. 12, no. 5, pp. 207–213, Oct. 2019, <https://doi.org/10.25103/jestr.125.23>.

- [4] M. H. Chamas, S. Amine, E. Gazo Hanna, and O. Mokhiamar, "Control of a Novel Parallel Mechanism for the Stabilization of Unmanned Aerial Vehicles," *Applied Sciences*, vol. 13, no. 15, Jan. 2023, Art. no. 8740, <https://doi.org/10.3390/app13158740>.
- [5] H. Mehdigholi and S. Akbarnejad, "Optimization of Watt's Six-Bar Linkage to Generate Straight and Parallel Leg Motion," *International Journal of Advanced Robotic Systems*, vol. 9, no. 1, Mar. 2012, Art. no. 22, <https://doi.org/10.5772/50917>.
- [6] M. S. Jo, J. K. Shim, H. S. Park, and W. R. Kim, "Dimensional Synthesis of Watt II and Stephenson III Six-Bar Slider-Crank Function Generators for Nine Prescribed Positions," *Applied Sciences*, vol. 12, no. 20, Jan. 2022, Art. no. 10503, <https://doi.org/10.3390/app122010503>.
- [7] J. Hu, Y. Sun, and Y. Cheng, "High mechanical advantage design of six-bar Stephenson mechanism for servo mechanical presses," *Advances in Mechanical Engineering*, vol. 8, no. 7, Jul. 2016, <https://doi.org/10.1177/1687814016656108>.
- [8] J. Alvarez-Cedillo, T. Alvarez-Sanchez, and M. Aguilar-Fernandez, "Design of a Watt Mechanism with Crossed Axes," in *Telematics and Computing*, Puerto Vallarta, Mexico, 2020, pp. 116–127, https://doi.org/10.1007/978-3-030-62554-2_9.
- [9] G. R. Gogate and S. B. Matekar, "Unified synthesis of Watt-I six-link mechanisms using evolutionary optimization," *Journal of Mechanical Science and Technology*, vol. 28, no. 8, pp. 3075–3086, Aug. 2014, <https://doi.org/10.1007/s12206-014-0715-0>.
- [10] B. Pira and I. Cunaku, "Synthesis of WATT and Stephenson Mechanisms six bar mechanism using Burmester Theory," *International Journal of Current Engineering and Technology*, vol. 7, no. 1, pp. 25–29, 2017.
- [11] Y. Liu and S. Yang, "Kinematic solution of spherical Stephenson-III six-bar mechanism," *Chinese Journal of Mechanical Engineering*, vol. 26, no. 5, pp. 851–860, Sep. 2013, <https://doi.org/10.3901/CJME.2013.05.851>.
- [12] R. Singh *et al.*, "Caster Walker GAIT Trainer (CGT): A robotic assistive device," *Robotics and Autonomous Systems*, vol. 159, Jan. 2023, Art. no. 104302, <https://doi.org/10.1016/j.robot.2022.104302>.
- [13] J. Wang, M. Yang, and Y. Huang, "The Kinematic Investigation of the Stephenson-III Spherical Mechanism with a Spherical Slider Containing a Spherical Prismatic Pair," *Applied Sciences*, vol. 13, no. 13, Jan. 2023, Art. no. 7454, <https://doi.org/10.3390/app13137454>.
- [14] S. Z. Ying, N. K. Al-Shammari, A. A. Faudzi, and Y. Sabzehmeidani, "Continuous Progressive Actuator Robot for Hand Rehabilitation," *Engineering, Technology & Applied Science Research*, vol. 10, no. 1, pp. 5276–5280, Feb. 2020, <https://doi.org/10.48084/etasr.3212>.
- [15] R. L. Norton, *Design of Machinery*, 6th edition. McGraw Hill, 2019.
- [16] V. Petuya, E. Macho, O. Altuzarra, C. Pinto, and A. Hernandez, "Educational software tools for the kinematic analysis of mechanisms," *Computer Applications in Engineering Education*, vol. 22, no. 1, pp. 72–86, 2014, <https://doi.org/10.1002/cae.20532>.
- [17] M. AlJaimaz, Z. AlMazidi, H. AlDousari, F. Ebrahim, D. AlZayyan, and E. G. Hanna, "Kinematic Analysis of a Variable Speed Deep Drawing Press Using GIM Software," presented at the The 9th World Congress on Mechanical, Chemical, and Material Engineering, Aug. 2023, <https://doi.org/10.11159/icmie23.142>.
- [18] V. H. M. Babu, "Theoretical Performance Comparison of a Robot Arm made by Aluminium Alloy and S2 Glass Fiber," *International Journal of Engineering*, vol. 4, no. 3, 2016.